Photosynthesis Research (2023) 156:113–128
https://doi.org/10.1007/s11120-022-00985-w

ORIGINAL ARTICLE

Regulation of light energy conversion between linear and cyclic electron flow within photosystem II controlled by the plastoquinone/quinol redox poise

Colin Gates[1,2,3,4] · Gennady Ananyev[1,2] · Shatabdi Roy-Chowdhury[5] · Petra Fromme[5] · G. Charles Dismukes[1,2]

Received: 31 May 2022 / Accepted: 9 November 2022 / Published online: 27 November 2022

Abstract

Ultrapurified Photosystem II complexes crystalize as uniform microcrystals (PSIIX) of unprecedented homogeneity that allow observation of details previously unachievable, including the longest sustained oscillations of flash-induced O_2 yield over > 200 flashes and a novel period-4.7 water oxidation cycle. We provide new evidence for a molecular-based mechanism for PSII-cyclic electron flow that accounts for switching from linear to cyclic electron flow within PSII as the downstream PQ/PQH_2 pool reduces in response to metabolic needs and environmental input. The model is supported by flash oximetry of PSIIX as the LEF/CEF switch occurs, Fourier analysis of O_2 flash yields, and Joliot-Kok modeling. The LEF/CEF switch rebalances the ratio of reductant energy (PQH_2) to proton gradient energy (H^+_o/H^+_i) created by PSII photochemistry. Central to this model is the requirement for a regulatory site (Q_C) with two redox states in equilibrium with the dissociable secondary electron carrier site Q_B. Both sites are controlled by electrons and protons. Our evidence fits historical LEF models wherein light-driven water oxidation delivers electrons (from Q_A^-) and stromal protons through Q_B to generate plastoquinol, the terminal product of PSII-LEF in vivo. The new insight is the essential regulatory role of Q_C. This site senses both the proton gradient (H^+_o/H^+_i) and the PQ pool redox poise via e^-/H^+ equilibration with Q_B. This information directs switching to CEF upon population of the protonated semiquinone in the Qc site $(Q^-H^+)_C$, while the WOC is in the reducible S2 or S3 states. Subsequent photochemical primary charge separation ($P^+Q_A^-$) forms no $(QH_2)_B$, but instead undergoes two-electron backward transition in which the Q_C protons are pumped into the lumen, while the electrons return to the WOC forming (S1/S2). PSII-CEF enables production of additional ATP needed to power cellular processes including the terminal carboxylation reaction and in some cases PSI-dependent CEF.

Keywords Photosystem II · Microcrystals · Oxygen evolution · Water-oxidizing complex · Kok model · Electron acceptors · VZAD

Introduction

Fifty years ago, the Joliot group first observed period-four oscillations in flash oxygen yield, paving the way for extensive studies of what was eventually discovered to be the catalyst known as the water-oxidizing complex (WOC) of photosystem II (PSII) (Joliot et al. 1969; Joliot and Joliot 1968). As these oscillations were seen to eventually decay to a steady-state oxygen yield, it was evident that the catalytic photo-cycle was subject to inefficiencies that competed with the successive accumulation of one-electron oxidized intermediates as the cycle advances. These inefficiency processes were first modeled by Kok and coworkers, who proposed a simple Markov model for the behavior of the WOC and mapped out the sequence of four one-electron photochemical

This article is dedicated to the memory of Professor Kenneth Sauer who made important contributions to understanding of the photosystems and the Z-scheme.

Also, we had a dedication to another friend and mentor to the authors, Prof. Ron Pace, who also passed away during the production of this paper and who served as an inspiration to the work. The dedication read. This work is dedicated to the memory of Professor Ronald Pace whose dogged questioning and insightful ideas inspired us to ask why, to delve deeper, and to always treat historical interpretations as conditional models.

✉ G. Charles Dismukes
dismukes@chem.rutgers.edu

Extended author information available on the last page of the article

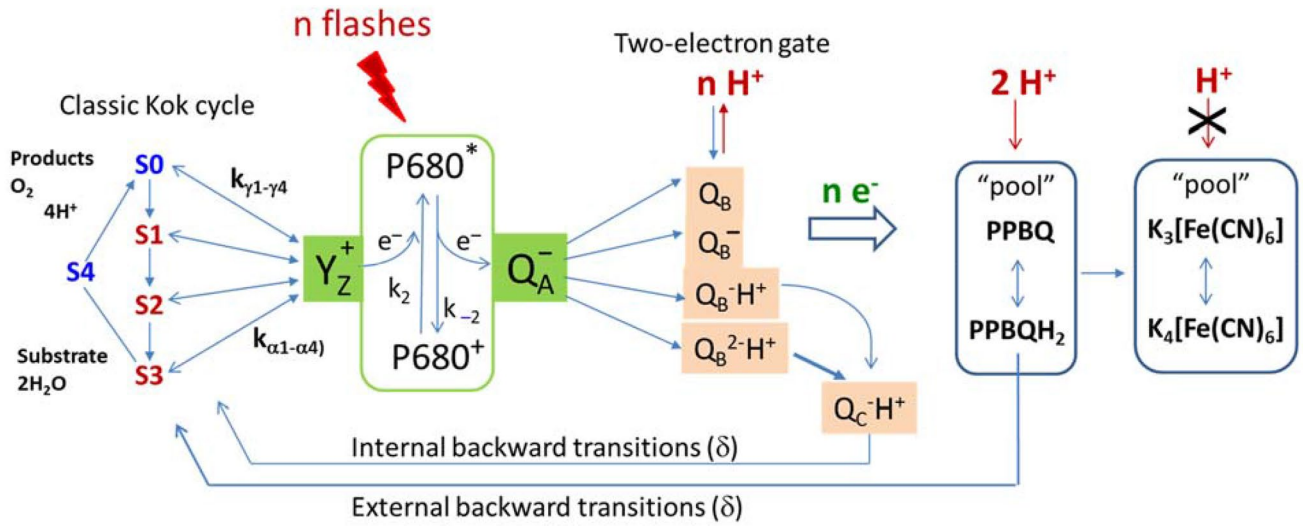

Scheme. 1 Rates and constraints in electron transfer within PSII microcrystals with controlled electron acceptors, showing electron return pathways

steps of the cycle well before the composition of the WOC was known (Kok et al. 1970). Kok's nomenclature is used today, Scheme 1**.** The catalytic site that produces O_2 and which stores these electron vacancies was later identified by EPR spectroscopy as a tetramanganese cluster (Dismukes and Siderer 1981). The primary (Q_A) and secondary (Q_B) electron acceptors that are required for stable charge separation were identified as plastoquinone (Crane et al. 1960; Amesz 1964) and the corresponding enzyme is known as the Photosystem II (PSII) water-plastoquinone oxidoreductase.

Following the publication of Kok's model, it became apparent through the study of other PSII-containing systems that this simple model did not adequately describe the activity of the WOC, and numerous other models were proposed to account for other inefficiencies, each adding layers of complexity to account for the numerous electron-transfer processes in PSII which may affect WOC operation (Meunier 1993; Vass and Cser 2009; Vass 2012; Pham and Messinger 2016; Lavergne and Junge 1993; Belyaeva et al. 2008; Bouges-Bocquet 1980; Dau 1994; Dau and Haumann 2007; Meunier and Burnap 1996; Schatz et al. 1988). A simple and effective improvement on Kok's algorithm was developed by Wraight and Shinkarev, and the Shinkarev model supplemented the original Kok inefficiency parameters, alpha (miss) and beta (double-hit), with two additional parameters delta (backward transition) and epsilon (inactivation) to increase the quality of model fits to data (Shinkarev 2005a, 2003, 2005b; Shinkarev and Wraight 1993b). These authors proposed that the efficiency of advancing through the WOC cycle varied with two flash steps depending upon the redox state of the quinone acceptors Q_AQ_B of PSII (Shinkarev 1996; Shinkarev and Wraight 1993a; Wraight 1979; Robinson and Crofts 1983). Earlier evidence for the predicted binary oscillations in O_2 yield from PSII has been sparse (Zhu et al. 2005; Rappaport et al. 2002; Lazár and Jablonský 2009). The development of more sensitive oximetry methods, Fourier data analysis, strontium biosynthetic substitution of calcium in PSII, and exogenous quinone acceptor supplementation allowed detection of binary oscillations in various living cells and their attribution to gating by the Q_AQ_B acceptors (Ananyev et al. 2016; Gates et al. 2016).

However, the Kok and Shinkarev models required symmetric matrix solutions in which photochemical misses and backward transitions occurred with equal probability on every oxidation state (S state) transition in the WOC cycle, in contrast to experimental evidence. The development of solutions for asymmetric Markov models allowed this limitation to be overcome and one such model denoted VZAD is employed herein (Vinyard et al. 2013). Consistent with experimental data, the VZAD model restricts the backward transitions and inactivation to the dark-unstable S2 and S3 states and produces the closest agreement with the experimental data to date. However, the four inefficiency parameters and their assignment to specific S state transitions involving the four S states remains a model with embedded assumptions that can either facilitate or confound the interpretation of data. To determine the actual microstates responsible for these inefficiencies experimental data should be used from more uniform PSII centers like PSII microcrystals (Ananyev et al. 2019), and to replace static Markov models with microkinetic models that predict real time-dependent rates (Mani et al. 2022; Belyaeva et al. 2019; Laisk and Oja 2018).

Herein we take the former approach and utilize PSII microcrystals to greatly reduce the structural heterogeneity

and possibly simplify the distribution of microstates that can form. We analyze the O_2 yields as a function of flash rate using a fast Fourier transform algorithm to time-resolve the activity of PSII. We demonstrate that the four WOC inefficiency parameters can be individually controlled by the choice of the terminal exogenous electron acceptor and its redox poise. We use different exogenous electron acceptors to equilibrate with the native Q_AQ_B/PQ system and from this learn how the acceptor regulates the flow of electrons from water and the reverse flow of electrons to the upper S states.

Materials and methods

PSII isolation. Core complexes comprised of PSII dimers were isolated from *Thermosynechococcus elongatus* as described in (Kupitz et al. 2014a, 2014b; Coe et al. 2015). The use of stereochemically ultrapure beta-dodecylmaltoside (β-DDM) (Glycon Biochemicals) as detergent was found to be important to the final homogeneity of these complexes. It was used at a fixed ratio of detergent to chl of 0.7% β-DDM to 0.5 mM chlorophyll (chl). The protein concentration was determined based on the chl concentration at a known ratio of 70 chlorophyll/PSII dimer. Tentacle ion exchange chromatography (Toyopearl) was used to purify PSII in a detergent micelle. Subsequently, 4 rounds of recrystallization were performed as follows. PSII was batch-crystallized at 0.5 mM chlorophyll concentration using PEG2000 as a precipitant and repeated 4 times after resolubilizing by dilution in fresh solution. The PEG concentration was decreased at each precipitation, using 7.5%, 6.5%, 5.5%, and 4.5% PEG for each sequential step. Crystallization buffer consisted of 100 mM PIPES at pH 7.0, 5 mM $CaCl_2$, 10 mM tocopherol and 0.02% β-DDM. The crystals used for these studies were previously determined by optical microscopy to be highly uniform 10–12 µm in diameter (Ananyev et al. 2019). These microcrystals are denoted PSIIX. Stabilizing buffer for measurements consisted of 100 mM PIPES at pH 7.0, 5 mM $CaCl_2$, 10 mM tocopherol, 20% PEG2000 and 0.02% β-DDM.

Oximetry. All O_2 measurements were performed on a homemade Pt-Ir Clark-type electrode covered by a thin membrane, the most recent generation of an instrument extensively developed by Dr. Ananyev (Ananyev and Dismukes 2005; Ananyev et al. 2016, 2017a, 2008). This membrane was previously demonstrated to prevent diffusion of added electron acceptors to the electrode surface. The applied reducing potential has previously been proven sufficient to avoid generation of hydrogen peroxide and together with the membrane prevent it from reaching the sample (Ananyev et al. 2016; Pham and Messinger 2014). All measurements were carried out under constant DC voltage bias without the use of an AC filter; thus, values returned are directly proportional to the current used to reduce O_2, and, by integration, the O_2 yield using Faraday's law ($4e^-/O_2$). Shading effects on the electrode were avoided by use of a sub-monolayer of crystals covering 30% of the electrode surface. Light was delivered across the visible spectrum using a high pressure Xe flash lamp (model ISSh-400). The flash duration at half maximum (FWHM) of this lamp was measured by a Si-pin photodiode (approximately 1 µs). The optical energy delivered was previously optimized for this system to deliver single turnover flashes as determined by saturation of the O_2 yield (> 95%) (Ananyev et al. 2019).

For all measurements, trains of single turnover flashes were used following dark incubation. Dark periods were chosen to allow the unstable S-state populations to decay to lower S-states which maximizes the signal to noise ratio of the oscillations. The flash trains were delivered with 1, 2, or 4 s between flashes with 10-min dark pre-incubation to allow decay of S2 and S3 populations unless otherwise specified. The timescale for decay of S2 and S3 were previously reported and strongly depend on the presence of electron acceptors that can autoreduce the S-states (Ananyev et al. 2019). Peak oxygen evolution (Yp) is defined as the oxygen yield on the flash resulting in the greatest quantity of oxygen production, i.e., flash 3 when the initial S1 population reaches S4 and S0. Oxygen evolution at steady-state (Yss) is defined as the average of the oxygen yield on the last 50 flashes of the train, when minimal oscillation is occurring and little decline occurs.

Two methods were utilized to analyze the time-dependent oscillations of flash O_2 yield data. Model-independent Fourier transformation of flash trains was performed to determine the distribution of frequencies of the oxygen yield (Ananyev and Dismukes 2005). Fourier transformation was performed using the GNU Science Library's C++ implementation of the FFTPACK fast Fourier transform library (Swarztrauber 1982). Where specified, the time-domain data of 100 flashes were broken up to the first 30 and last 70 flashes (or more). For visual comparison of FFT output data, where specified a cubic spline with resolution 0.001 cycles/flash was applied using the GNU Science Library's C++ implementation of the *cspline* interpolation algorithm (Steffen 1990).

Model-dependent analysis was carried out by fitting the O_2 yields of each flash train to a four-parameter Joliot-Kok model of the WOC cycle, denoted VZAD, as previously described (Ananyev et al. 2016; Vinyard et al. 2013). VZAD minimizes the root-mean-squares deviation between the data and calculated O_2 yield to obtain the four Markov inefficiency parameters and the initial (dark) S-state populations (illustrated in Figure S1). The current version of the VZAD model is available at http://chem.rutgers.edu/dismukes-software. To illustrate the necessity of the four

parameters to adequately model this data we have added to the SI fits to an example data set which was processed using the standard VZAD package (Figure S2) and the same data processed using a constrained VZAD model in which either alpha, beta, delta, or epsilon were omitted (Figure S3, using the same data set). In all cases, the fits did not come close to approximating the data, also as shown in numerous previous publications.

The synthetic quinone *para*-phenylbenzoquinone (PPBQ) was obtained from Aldrich Chemical Co. (originally 98% purity) and further purified by double recrystallization in ethanol. It was subsequently dissolved in dimethyl sulfoxide (DMSO) at 20 mM concentration, after which further dilution into crystal samples was carried out as needed for experiments. $K_3Fe(CN)_6$ (potassium ferricyanide, abbreviated FeCN) was obtained from Sigma-Aldrich (99% purity). Near-total oxidation of both electron acceptor stocks (quinone form of PPBQ rather than quinol; ferricyanide as opposed to ferrocyanide) was established previously (Ananyev et al. 2016).

Results

Flash periods in O_2 oscillations. PSIIX microcrystals show extended oscillations in flash-induced O_2 yield (Ananyev et al. 2019). Herein, we demonstrate that PSIIX microcrystals can produce up to 50 periods of oscillations extending over 200 single turnover flashes (Fig. 1A). Oscillations extending over periods greater than approximately 80 flashes have only been observable in the microcrystal system to date. Fourier transformation of these data, all 200 flashes, is shown in Fig. 1B and illustrates the range of flash periods that are permissive of O_2 evolution.

The decay of the oscillations does not exhibit a single exponential temporal dependence indicating multiple phases contribute. To examine these temporal phases, we performed Fourier analysis over successive flash intervals to extract the intrinsic catalytic cycle frequencies that are permissive of O_2 production (Fig. 2A). The Fourier transform of the first 30 flashes in a train (Fig. 2B) shows a broad central peak centered on a cycle frequency of 0.24 equal to 4.14 flashes per cycle (just longer than the ideal 4 flash cycle). The width of the distribution represents the spread in number of flashes that produce O_2. The full width at half maximum (FWHM) of the distribution centered near period-4 for the first 30 flashes is 0.09 cycles per flash. This distribution narrows in the remaining 70 flashes (Fig. 2D), by threefold to a FWHM of just under 0.03 cycles per flash. The overall likelihood of inefficiencies causing a non-period-4 cycle is thus much lower in this second phase following illumination than during this initial phase starting from dark adaptation.

The Fourier spectrum of flashes 31 to 70 (Fig. 2D) reveals two prominent peaks at approximately 0.25 cycles per flash (period-4) and 0.50 cycles per flash (period-2). The period-4 peak is much closer to the ideal value for a four-flash WOC cycle, reflecting improved efficiency compared to the first 30 flashes. The period-2 peak has been observed previously in some living systems and assigned to gating of electron/proton flux at the Q_B acceptor site (Ananyev et al. 2016; Gates et al. 2016) as previously predicted (Shinkarev 1996; Shinkarev and Wraight 1993a; Wraight 1979; Robinson

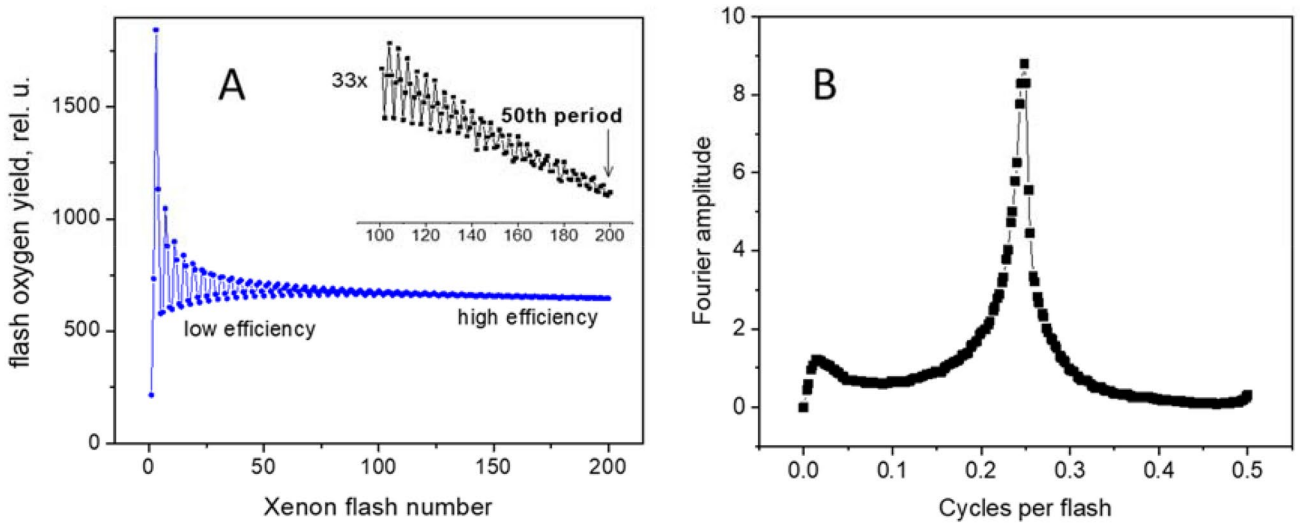

Fig. 1 **A** Oscillations in oxygen yield from PSIIX microcrystals from a train of 200 flashes each 1 µsec long at 0.5 Hz detected by a membrane-covered (Clark-type) electrode. The resulting current pulse is integrated to obtain the yield of O_2 per flash. Inset shows the last 100 flashes magnified vertically 33-fold. **B** Fourier transform of (**A**), shown with cubic spline applied. Data shown are the average of 5 technical replicates. Electron acceptors used were 4 mM FeCN and 200µM PPBQ

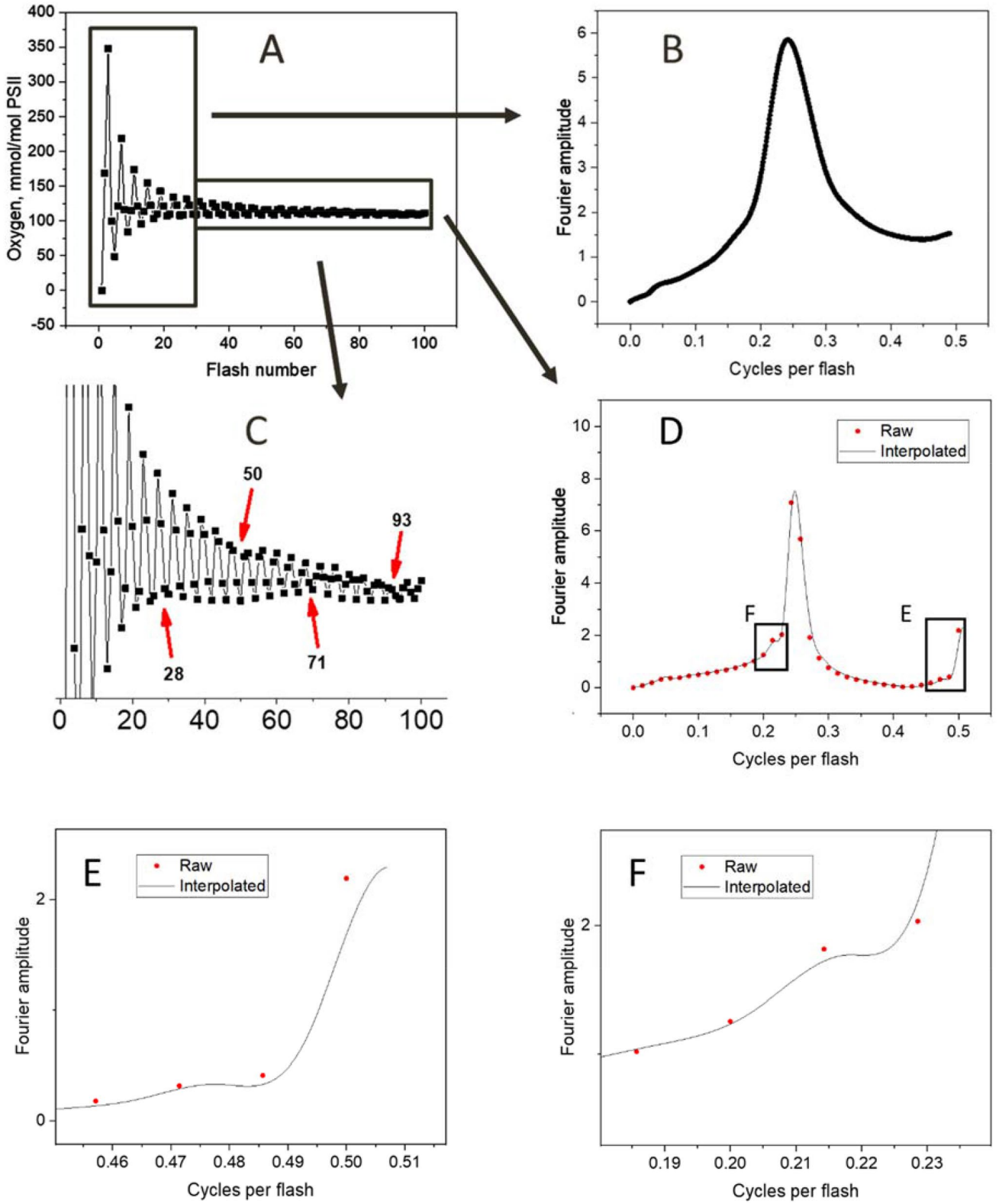

Fig. 2 **A** Oxygen yields from a train of 100 single turnover flashes at 0.5 Hz applied to a PSII microcrystal sample supplied with 200 µM PPBQ and 4 mM FeCN. **B** Splined Fourier transform of flashes 1–30 of the flash train. **C** Expansion of the raw data in (**A**) shows crossover of oscillations reflecting the different WOC cycle periods. **D** Fourier transform of flashes 31–100 with peaks marked; red points are raw data with a Fourier transform of a rectangular window of equivalent number of data points subtracted to remove window artifact, while the black trace is a spline interpolation between points. In addition to the narrower central Fourier peak at period 4.14, prominent auxiliary peaks are observed at E) 0.5 cycles (period 2) and F) 0.21 cycles (~ period 4.7)

and Crofts 1983). Although present in the first 30 flashes, it increases to almost a third that of the major period-4 peak on the following 70 flashes. Expansion of the O_2 yield data for flashes 31–100 given in Fig. 2C shows crossover of oscillations reflecting additional cycle periods that contribute to the oscillations. The corresponding Fourier transform in Fig. 2D, 2E and 2F shows that in addition to the two prominent peaks there is a significant shoulder observed at F) 0.21 cycles (~period 4.7). Another less prominent feature consistently appears in all traces at approximately 0.05 cycles (every 22 flashes shown in Fig. 2C), but unlike the period-4, -4.7 and -2 oscillations it exhibits greater temporal variability (detailed in Fig. S4).

Slowing the flash rate to allow the slower decaying populations of S states to contribute to the oscillations in O_2 production reveals additional features of the WOC cycle (Fig. 3). First, the oxygen yield increases substantially at lower flash rate. Second, there is an approximate inverse relationship between the period-4 FT amplitude, shown in Fig. 3B, and the steady-state oxygen yield, shown in Fig. 3A. This is to be expected as the delivery of PPBQ or FeCN acceptor inside the microcrystals is known to limit the yield of oxygen (Ananyev et al. 2019). Third, the period-2 and period-4 FT features change differently with flash rate as seen in Fig. 3C, D where it is seen that at slower flash rates the period-2 distribution broadens substantially more than the period-4 distribution. This attribute indicates that that the timescale of the period-2 process occurs on the same timescale as the flash frequency (1 to 4 s), during which the

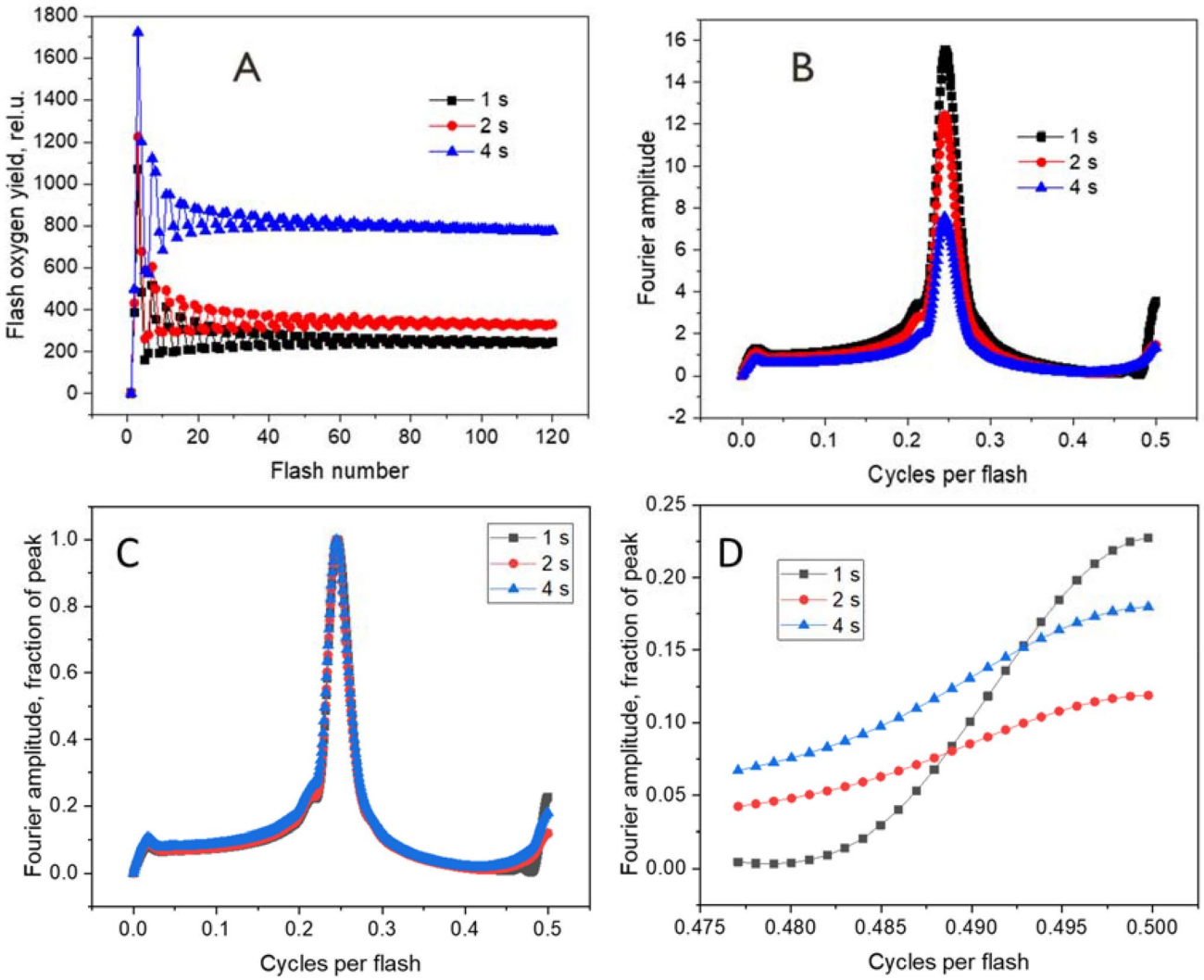

Fig. 3 **A** Oxygen yield from single turnover Xenon flashes applied to a PSIIX microcrystal sample supplied with 200 µM PPBQ and 4 mM FeCN. The flash trains were delivered with 1, 2, or 4 s between flashes as denoted. **B** Fourier transform of the region of flashes from number #31 to #100 in (**A**), cubic splined data. **C** Fourier transform plots from (**B**) normalized to a peak height of 1 at period-4. **D** Expansion of the period-2 peak region in (**C**)

period-4 process is unaffected (i.e., the WOC transitions are faster).

Relationship between WOC Periods and Acceptor Availability

Using many more flashes enables monitoring of consumption of the finite pool of added electron acceptor. Using this approach, we previously observed three phases in the loss of steady-state O_2 yield (Yss) as the added PPBQ and FeCN pools are consumed and their equilibration with the redox states of the native electron acceptors, Q_A and Q_B, is lost (Ananyev et al. 2019). Figure 4A shows that with only FeCN as acceptor, only two temporal phases are seen in the loss of O_2 yield, denoted as the FeCN-replete and FeCN-limited phases. Using both acceptors, three phases are observable (Fig. 4B) denoted as PPBQ-as-acceptor, FeCN-as-acceptor, and acceptor-limited, in order of consumption. Period-4 oscillations stay relatively constant through the first two phases, until the FeCN-limited phase is reached (Fig. 4B), regardless of whether or not PPBQ is used with FeCN. The steady-state yield of O_2 (Y_{ss}) is twice as large when both electron acceptors is used. At the end of the third phase of acceptor consumption the Period-4 amplitude does not reach zero even though Y_{ss} does. This is likely due to a combination of recovery of available electron acceptors during the longer dark adaptation time prior to flashing and minor use of dissolved O_2 as an inefficient terminal electron acceptor in PSIIX (Ananyev et al. 2019).

The period-2 amplitude has different behavior than does period-4 as it exhibits three distinct phases in parallel with the three phases of Y_{ss}, regardless of the presence or absence

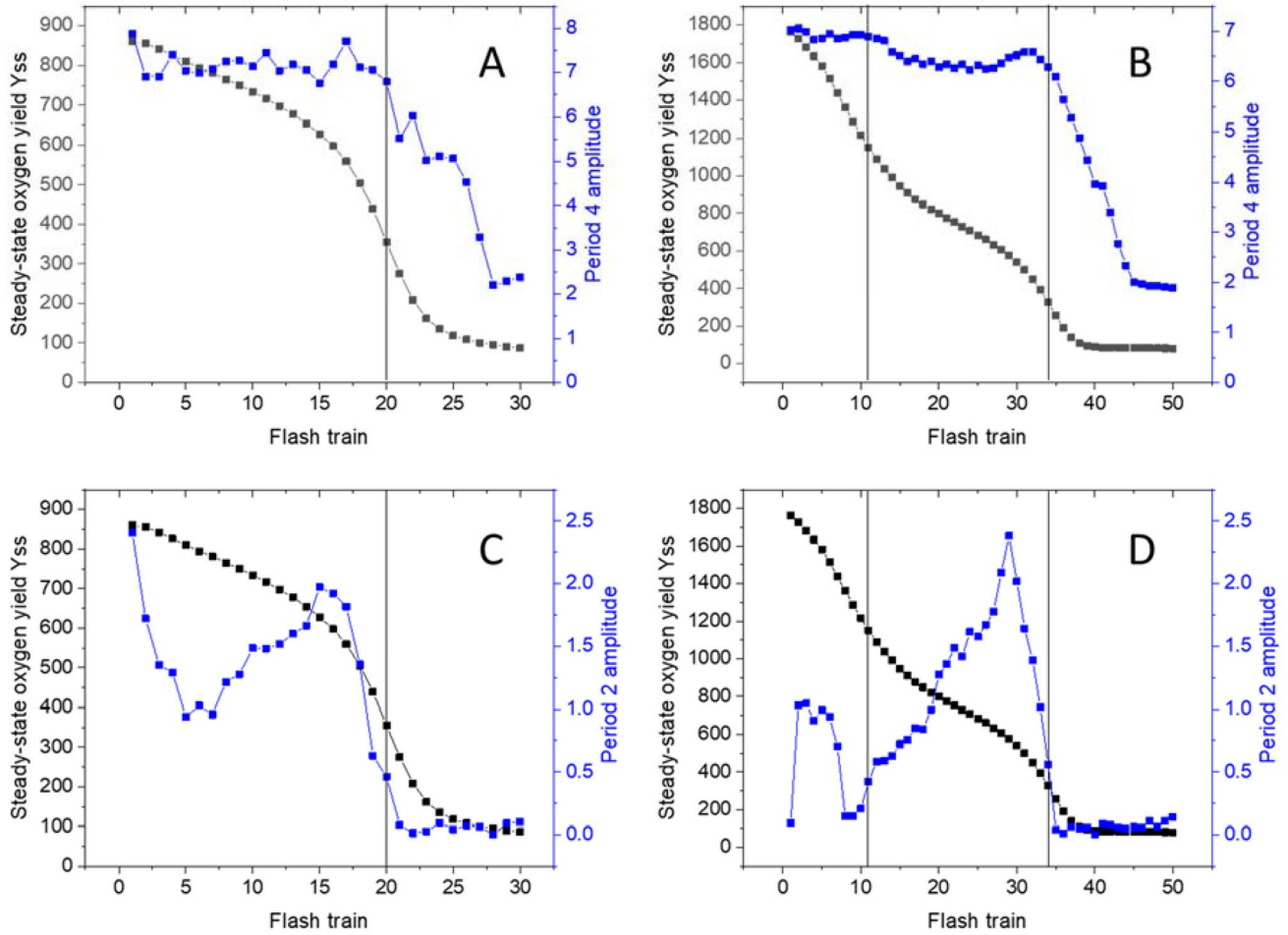

Fig. 4 The Fourier peak amplitude of the period-4 (**A** and **B**) and period-2 (**C** and **D**) peaks obtained from flashes #31 to #100 within each train of 120 flashes (in blue ■), and the average oxygen flash yield Y_{ss} for each train (in black ■) over a series of flash trains during which electron acceptor is consumed to a level of inactivity. Data shown are representative of multiple data sets ($n = 5$). Sample supplemented with: (**A** and **C**) 4 mM FeCN; (**B** and **D**) 200 µM PPBQ and 4 mM FeCN. Vertical lines denote three approximate phase transitions in which the exogenous electron acceptors are consumed. Each flash train has 120 single turnover flashes delivered at 0.5 Hz and is preceded by dark adaptation for 10 min. (Color figure online)

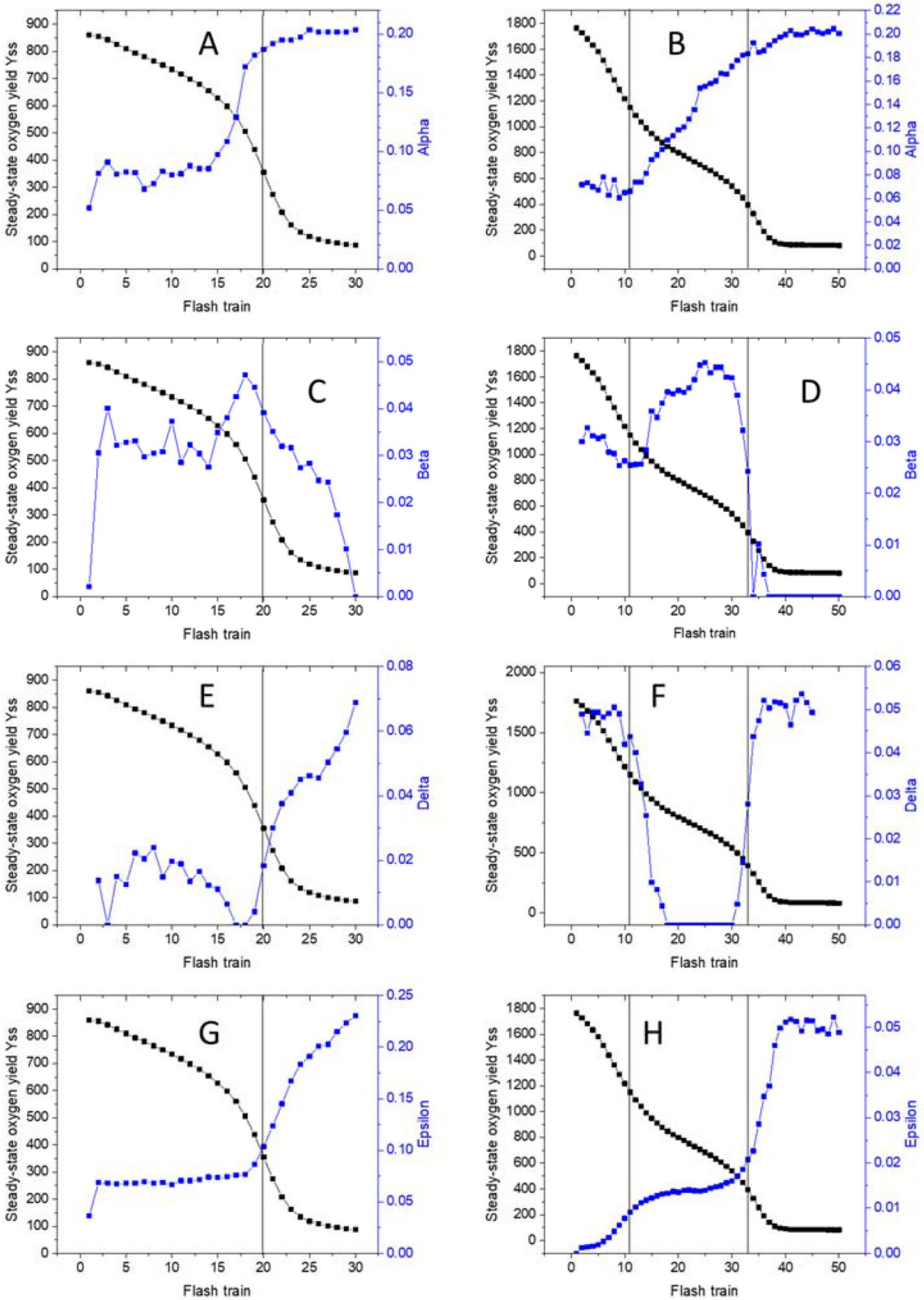
A
Steady-state oxygen yield Yss
Alpha
Flash train
B
Steady-state oxygen yield Yss
Alpha
Flash train
C
Steady-state oxygen yield Yss
Beta
Flash train
D
Steady-state oxygen yield Yss
Beta
Flash train
E
Steady-state oxygen yield Yss
Delta
Flash train
F
Steady-state oxygen yield Yss
Delta
Flash train
G
Steady-state oxygen yield Yss
Epsilon
Flash train
H
Steady-state oxygen yield Yss
Epsilon
Flash train

◂**Fig. 5** Changing of the Joliot-Kok inefficiency parameters in PSIIX as flashes accumulate electrons and protons in two types of electron acceptor pools. O_2 yields are also shown from flashes 31–100 of individual flash trains. In black (■), the steady-state yield (Yss) from sequential flash trains. In blue (■), the four inefficiency parameters obtained from each flash train via VZAD model fits. Data shown are representative of multiple data sets ($n=5$). (**A**, **C**, **E**, and **G**) Sample supplemented with 4 mM FeCN; (B, D, F, and H) Sample supplemented with 200 µM PPBQ and 4 mM FeCN. (A and B) alpha miss parameter; (C and D) beta double-hit parameter; (**E** and **F**) delta backward transition parameter; (**G** and **H**) epsilon inactivation parameter. Vertical lines denote approximate acceptor phase transitions. (Color figure online)

of PPBQ (Fig. 4C, D). With the exception of the first train (FeCN + PPBQ), the trend in period-2 is the same in both cases, decreasing during phase 1, increasing during phase 2 and decreasing to zero during phase 3. The exception on the first train that occurs with FeCN + PPBQ is reproducible ($n=5$) and is believed to be attributable to the ability of PPBQ to equilibrate with the native PSII acceptors more rapidly or more fully than does FeCN alone. The period-2 feature appears to be strongly linked to the production and retention of semiquinone in the Q_B site. Plastosemiquinone binds to the Q_B site with highest affinity compared to the oxidized plastoquinone form, while the fully reduced plastoquinol form has the lowest binding affinity (Satoh et al. 1992). This suggests that phase 1 is associated with the removal of the most populated form of the intrinsic electron acceptor as the flashes continue, e.g., the loss of the semiquinone form of Q_B^-. As the flashes continue, phases 2 and 3 would then be attributable to microstates in which the B site is occupied by an oxidized plastoquinone and finally plastoquinol, respectively. See the Discussion for further details.

Analyzing PSIIX regulation using Joliot-Kok parameters and the VZAD model

Using PSIIX crystals, the quality of oscillations in oxygen yield from individual flash trains is high enough that, in addition to the model-independent Fourier analysis, fitting to a Joliot-Kok model can be applied even as the electron acceptor is consumed and the O_2 yield decreases. We fitted flashes 31–100 of each train using the VZAD algorithm (Fig. S1), which produces excellent fits with the smallest residuals, as seen in Fig. S2. This section of the train was selected because, in keeping with the acceptor diffusion limitation observed in Fig. 3, the preceding section is dominated by acceptor limitation resulting from the diffusion time for oxidized acceptor to reach the crystal interior exceeding the dark time between flashes. In this section of the train the exterior of the crystal has stable access to the acceptor pool. The sluggish response on flashes 1 to 30 results in a 4 times larger width of the period-4 oscillations.

The dependence of the four inefficiency parameters as a function of the consumption of electron acceptor is shown in Fig. 5 for the two-electron acceptor choices. Similarly, the initial S-state populations following dark adaptation were obtained by fitting the oscillations from the first 30 flashes of each train using VZAD, as shown in Fig. 6.

As a general observation when FeCN is the sole added electron acceptor, the four inefficiency parameters each have two regions that change in parallel with the two phases of consumption of FeCN, as shown in Fig. 5 A,C,E,G. Misses (alpha), backward transitions (delta), and inactivations (epsilon) all follow the same general trend with constant values initially, until the next phase occurs whereafter there is an inverse relationship with the oxygen yield as the FeCN is depleted. In the presence of only FeCN acceptor, the O_2 yield is initially half that with the two-electron acceptors and rapidly decreases in the next phase. The sample undergoes frequent inactivation (epsilon) that starts at 7% per WOC cycle in the first phase and rises to 22% at the end of the final phase where only O_2 should be the remaining electron acceptor. There is either insufficient plastoquinone to populate the Q_C site or it does not equilibrate with FeCN when there is no added PPBQ. Hence, the rise of the backward transition (delta) and the period-2 Fourier peak in the latter half of the first phase are interpreted as associated with the progressive population of the Q^-_B semiquinone form during illumination which persists in the dark after each flash train. See Table 1 and the Discussion for additional rationale. In the next illumination phase, Q^-_B is replaced by the reduced QH_{2B} quinol state which accumulates in the dark after each flash train.

In the presence of PPBQ + FeCN the progressive population of three microstates seen in the O_2 flash yield (Fig. 4) is accompanied by the same three temporal phases for each of the four inefficiency parameters (Fig. 5 B,D,F,H). The major change vs FeCN alone is a twofold increase in O_2 yield and a 4 to fivefold decrease in inactivation owing to the efficient capture of electrons by PPBQ. In both acceptor cases, we can thus directly link inactivation to the redox poise of an internal (native) electron acceptor in equilibrium with the exogenous acceptor pool, in agreement with our earlier assignment (Ananyev et al. 2019). During the PPBQ-dominated first phase (to about train 11), the misses are low, comparable to that seen with FeCN alone, which indicates they are intrinsic to PSIIX and not due to insufficient acceptor. During the next phase (to about train 33), when $PPBQ^-$ accumulates and presumably equilibrates with the Q_A and Q_C sites the misses rise continuously until in phase 3 they reach the same limiting value as observed with FeCN alone. Reduced $PPBQH_2$ does not accumulate in the PSIIX crystal or micelle as it is oxidized by excess FeCN. In the presence of PPBQ + FeCN (Fig. 5F), backward transitions exhibit a remarkable response, toggling from high to

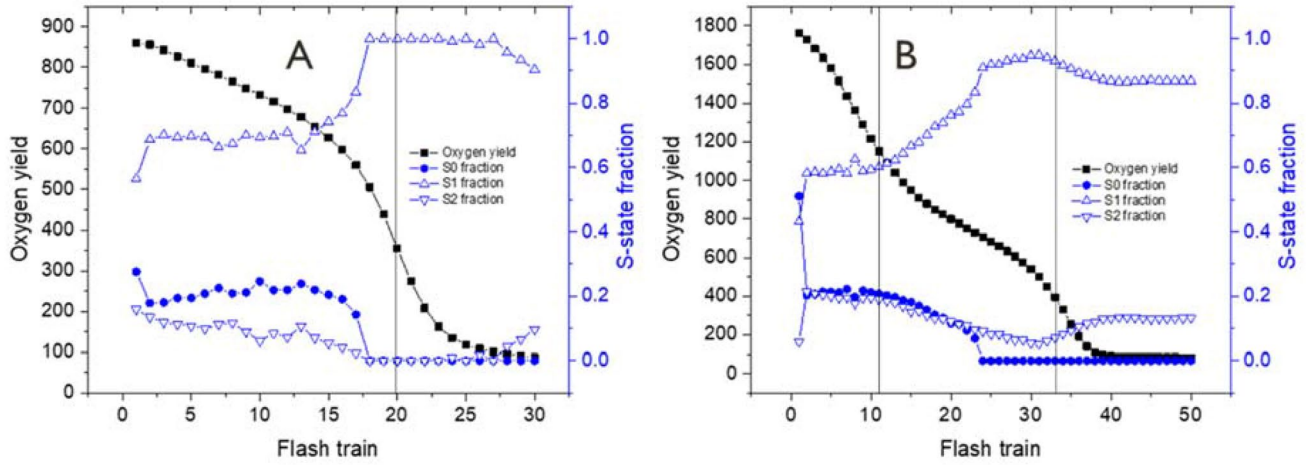

Fig. 6 The initial dark-adapted S-state population fractions as obtained from fits of the first 30 flashes of each flash train for 50 trains. The O_2 flash yields are shown from those flash trains. In black (■), the steady-state yield (Yss) from sequential flash trains. In blue (● Δ ▽), S state population fractions obtained from each flash train via VZAD model fit. The S3 population was omitted due to comprising less than 1% at all points. Data shown are representative of multiple data sets ($n=5$). **A** Sample supplemented with 4 mM FeCN; **B** Sample supplemented with 200 µM PPBQ and 4 mM FeCN. (Color figure online)

Table 1 Model of the microstates on the electron acceptor side of dark-adapted PSIIX microcrystals as their populations redistribute in response to flashes and short-term dark adaptation between trains. The flashes result in the consumption of the added electron acceptor (EA = FeCN or PPBQ + FeCN) by reduction and the generation of protons. The fraction of centers that perform LEF decreases while CEF increases as the acceptors are consumed. This scheme is a model also for what happens upon chemical reduction of the PQ pool in vivo. The three temporal phases refer to the consumption phases of electron acceptors described in Figs. 4, 5, and 6. During illumination, denoted by arrows→, the populations change as noted due to both e^- and H^+ transfer. The relative change in PSII-CEF is denoted by arrows (↓↑) or 0 for no effect, before and after illumination events. Q_C refers to a regulatory site for binding plastoquinone (native) or PPBQ. The microstates containing $(QH_2)_B$ may actually be $(empty)_B$ since the affinity for QH_2 is much lower than Q. In the scheme, the upper line of quinones refers to Q_B and the lower line to Q_C; the color of the Q_C quinone refers to whether CEF is proceeding

Phase 1 Oxidized acceptor	Phase 2 Depleted acceptor	Phase 3 Reduced acceptor	Added Electron Acceptors (EA)
$Q^-_B \rightarrow * \rightarrow Q_B + 2EA^-$ CEF 0→0	$Q_B \rightarrow Q^-H^+_B$ CEF 0→↑	$Q^-H^+_B \rightarrow QH_{2B}$ CEF↑→↑↑	FeCN
$Q_BQ^-_C \rightarrow Q^-_BQ^-H^+_C$ CEF↑→↑↑	$Q^-_BQ^-H^+_C \rightarrow Q_BQ_C + PPBQH_2$ CEF↑↑→↓↓	$Q_BQ_C \rightarrow Q^-_BQ^-H^+_C$ CEF 0→↑↑	PPBQ + FeCN

zero to high again in the three successive phases. Backward transitions (delta) and period-2 oscillations are initially high in phase 1, suggesting that as the semiquinone $PPBQ^-$ accumulates it can transfer an electron to form both of the native semiquinones (Q^-_B and Q^-_C, with or without H^+), as summarized in Table 1. This microstate has the largest delta parameter.

As phase 2 begins, both the period-2 and backward transition drop to zero. This is assigned to the replacement of the native semiquinones with their oxidized forms as these are oxidized either by excess PPBQ or native PQ, as summarized in Table 1. To explain why this happens only when there are semiquinones in both the B and C sites, we postulate it has to do with destabilization by charge repulsion, as the individual semiquinones have high binding affinity compared to the Q and QH_2 forms. As phase 2 continues the continuous recovery of the period-2 FT peak occurs indicating accumulation of Q^-_B semiquinone until at the beginning of phase 3 the two native semiquinones are again repopulated, as summarized in Table 1. This microstate has again the highest delta parameter. However, this state can no longer be oxidized by the lower concentration of remaining oxidized PPBQ which has been greatly diminished as the FeCN concentration has dropped by consumption.

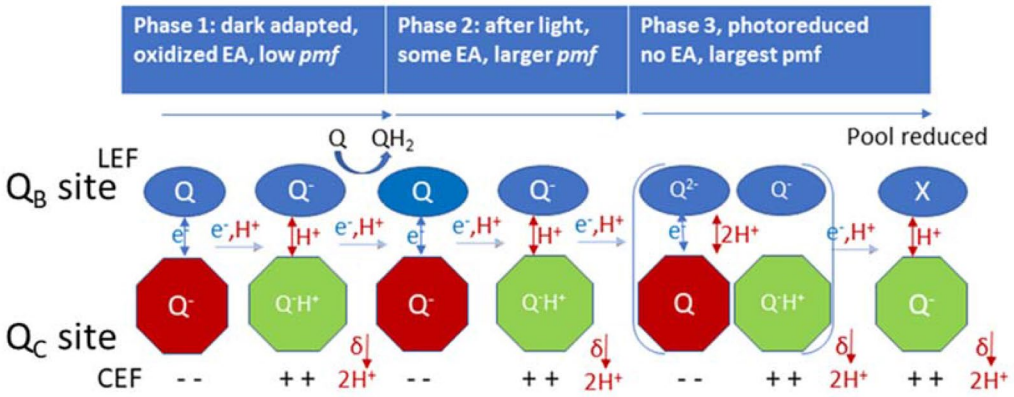

Phase 1 Oxidized acceptor	Phase 2 Depleted acceptor	Phase 3 Reduced acceptor	Added Electron Acceptors (EA)
$Q^-_B \rightarrow * \rightarrow Q_B + 2EA^-$ CEF 0→0	$Q_B \rightarrow Q^-H^+_B$ CEF 0→↑	$Q^-H^+_B \rightarrow QH_{2B}$ CEF↑→↑↑	FeCN
$Q_BQ^-_C \rightarrow Q^-_BQ^-H^+_C$ CEF↑→↑↑	$Q^-_BQ^-H^+_C \rightarrow Q_BQ_C + PPBQH_2$ CEF↑↑→↓↓	$Q_BQ_C \rightarrow Q^-_BQ^-H^+_C$ CEF 0→↑↑	PPBQ + FeCN

Scheme. 2 Model of the microstates on the electron acceptor side of dark-adapted PSIIX microcrystals as their populations redistribute in response to flashes and short-term dark adaptation between trains. The flashes result in the consumption of the added electron acceptor (EA = FeCN or PPBQ + FeCN) by reduction and the generation of protons. The fraction of centers that perform LEF decreases while CEF increases as the acceptors are consumed. This scheme is a model also for what happens upon chemical reduction of the PQ pool in vivo. The three temporal phases refer to the consumption phases of electron acceptors described in Figs. 4, 5, and 6. During illumination, denoted by arrows→, the populations change as noted due to both e^- and H^+ transfer. The relative change in PSII-CEF is denoted by arrows (↓↑) or 0 for no effect, before and after illumination events. Q_C refers to a regulatory site for binding plastoquinone (native) or PPBQ. The microstates containing $(QH_2)_B$ may actually be $(empty)_B$ since the affinity for QH_2 is much lower than Q. In the scheme, the upper line of quinones refers to Q_B and the lower line to Q_C; the color of the Q_C quinone refers to whether CEF is proceeding

Discussion

The three temporal phases observed in the loss of O_2 evolution as the terminal acceptors are consumed (with both FeCN and FeCN + PPBQ) were previously described and analyzed in terms of peak positions, and integrated electron capacities (Ananyev et al. 2019). These features were attributed to the titration of two internal electron acceptors within PSII that equilibrate with the added terminal acceptor pool to control the yield of O_2. Under the assumption of equilibrium between these internal acceptors and the terminal acceptor pool, these internal electron acceptors should possess increasingly more positive reduction potentials, either $(Q/Q^-)_A$ and $(Q/Q^-)_B$, or $(Q/Q^-)_B$ and $(Q^-/Q^{2-})_B$, with the Q_C proposed regulatory quinone site within PSII as an plausible alternate pathway diverging from the terminal acceptor pool (Hasegawa and Noguchi 2014; Huang et al. 2016; Guskov et al. 2009; Yadav et al. 2014).

Herein we have added the behavior of the WOC cycle periods from Fourier analysis and the Joliot-Kok inefficiency parameters obtained from best fits to the flash O_2 yields using VZAD. These additional layers of information now show that the backward transition parameter is an indispensable term to account for both the steady-state O_2 yield and its transient (non-equilibrium) oscillations when starting from a dark-adapted state. Taking into account both measures of the O_2 flux and the inefficiency parameters, we propose a more complete model that incorporates the backward transition as the mechanism responsible for cyclic electron flow *within* PSII. This model is shown in Scheme 2. To construct this model, we find it necessary to include a regulatory site within the acceptor side (Q_C) that can bind zero or one-electron (quinone or semiquinone, not quinol (Manoj et al. 2021)). In this model, the Q_C site serves as a redox signal for switching between linear electron flow (LEF) and cyclic electron flow (CEF) within PSII.

In this model, the backward transition is triggered by the one-electron reduced form of the regulatory site Q_C^- (semiquinone C). VZAD predicts this occurs 5% of the time (probability delta = 5%) in phase 1 in all centers. Occupation of the Q_C site is limited in PSIIX, which is commonly attributed to the relatively low affinity of quinone head groups (Krivanek et al. 2007; Hasegawa and Noguchi 2014; Huang et al. 2016; Manoj et al. 2021; Guskov et al.

2009; D Lambreva et al. 2014). This site is thought to be reducible by only one electron to form the semiquinone which binds more tightly, as measured by the reduction of molecular oxygen to superoxide radical (Yadav et al. 2014). Quinol in the Q_C site has not been reported so far to our knowledge. Linear electron flow proceeds through the formation of the $(QH_2)_B$ plastoquinol in native cells, while in PSIIX it can bypass Q_B in some or all centers directly to added PPBQ + FeCN. As FeCN gets consumed by reduction from Q_A^- the remaining bound semiquinone $PPBQ^-$ that forms will be longer-lived and can equilibrate with Q_B to form Q_B^-. The semiquinone is the thermodynamically more stable redox form that binds to the B site (Causmaecker et al. 2019). However, in the centers with both Q_B^- and Q_C^-, the two semiquinones are expected to comproportionate to form the quinol form of $(QH_2)_B$ and the oxidized Q_C site, especially when protons are available. This reaction will in turn eliminate backward transitions during phase 2 as predicted by the model of Scheme 2 (Yao et al. 2018). The complete lack of backward transitions during this phase makes a compelling case for the necessity of involvement of the Q_C site, as if backward transitions were solely regulated at either the Q_A or Q_B site then one would expect a proportional increase in backward transitions over time as the relevant site is blocked, following kinetics similar to those observed for misses, which include recombination via the classical pathway. Under continued illumination throughout phase 2, the FeCN and PPBQ pools form more ferrocyanide and reduced $PPBQH_2$, which further blocks oxidation of $(QH_2)_B$. This blockage causes a proportionate increase in misses throughout phase 2. At the end of phase 2, accumulation of QH_{2B} shifts the equilibrium with oxidized (quinone) Q_C back to the production of semiquinone in the C site. Finally, as these reduced forms continue to accumulate the chemical exchange pathway for replacement of the B site with the available quinone slows further and the system stops producing any O_2.

PSII-CEF has been hypothesized for decades (Falkowski et al. 1986; Prasil et al. 1996; Feikema et al. 2006; Shinopoulos and Brudvig 2012). It was previously proposed to be the functional purpose of backward transitions predicted by Joliot-Kok models that account for both the loss of average O_2 yield and the damping of transient O_2 oscillations and of PSII variable fluorescence (Ananyev et al. 2016, 2017b). The mechanism has not been definitively established previously, beyond the observation that it involves electrons that reach Q_B before returning to the donor side. Alternative mechanisms include an electron pathway back to P680 without directly entering the WOC that goes through cytochrome b559 (Takagi et al. 2019; Shinopoulos and Brudvig 2012). This pathway is a less plausible explanation for the preceding data since it is a one-electron only pathway and operates on a slower (seconds) timescale than the recombination reactions of Y_z^+ and WOC with Q_B^-. Additionally, the cytochrome b559 model does not explain the major energy-transducing benefit of PSII-CEF, the production of a transmembrane proton gradient (Kedem et al. 2021).

A feasible molecular mechanism for PSII-CEF that is consistent with our findings is given in Scheme 2. Functionally, this mechanism contributes three benefits to photosynthetic organisms: 1) it converts redox energy accumulated in the reduced PQH_2 pool into a *pmf* across the thylakoid membrane and ultimately into ATP, 2) it restores photochemical quenching by opening closed PSII centers that have over reduced PQH_2 pools, and 3) it protects against oxidative damage caused by the two most reactive S-states (S3 and S4). The first of these functions is essential for the terminal carboxylation reaction which has an ATP requirement that is not met by LEF alone. The proposed mechanism operates during the two slowest S-state transitions starting from the pre-flash microstates S2 (or S3) $Q_B^-Q_C^-H^+$ by performing a $2e^-$ backward transition after the flash. We postulate that the captured proton, which originates from the stroma, can equilibrate between the two semiquinones $(Q_B^-$ and $Q_C^-)H^+$ depending upon the choice of pathway, LEF of CEF, respectively. After the next flash (producing $Yz^+Q_A^-$ by charge separation) the (third) electron is delivered to Q_A^- and an additional proton from the stroma is taken up and equilibrates between $(Q_B^-$ and $Q_C^-)H^+$. The resulting microstate is S_2(or S_3)$Y_Z^+Q_A^-Q_B^-Q_C^-$ $2H^+$, and is the precursor to the backward transition. The two protons are proposed to transfer to the aqueous lumenal space during the two-electron recombination that ultimately reduces Y_z^+ and manganese in the WOC (either $S_2 \rightarrow S_1$ or $S_3 \rightarrow S_2$). Although the intermediate carriers for returning the protons and electrons are unknown, some candidates for the electron pathways include: $Q_B^- \rightarrow Y_z^+ \rightarrow$ WOC and $Q_C^- \rightarrow Y_D^+$(tyrosine-D) $\rightarrow$WOC. The latter pathway has been observed previously without a clear proton destination proposed (Jenson and Barry 2009).

The WOC turnover rate and efficiency is pH-dependent, though this is sometimes attributed to misses rather than backward transitions (Pham et al. 2019). Misses, however, are distinct from backward transitions as they occur on all S-state transitions, do not result in a change of WOC oxidation state, nor are they proton-coupled (Mani et al. 2022). The observed miss rate increases during illumination as reduced $PPBQH_2$ accumulates, which provides additional evidence that redox regulation of charge recombination contributes significantly to PSII photoprotection. However, it must be noted that misses are exclusively energy-dissipative and this form of regulation is simple feedback, in contrast to regulation of energy-conversing backward transitions which utilize a regulatory site (Q_C) to "read" the redox poise of the Q_A-Q_B-PQ pool. It stands to reason that, as PSII-CEF

is posited to generate proton gradient, and thus requires proton release in the lumen at an undetermined site, the proton gradient would also be a regulator of the PSII-CEF pathway, though likely a less significant determinant than the redox state of the PQ pool. The magnitude of relative effects cannot be definitively established from this study, however, as to observe acceptor regulation at this resolution it is necessary to use isolated and purified PSII in an environment where protons are rapidly removed and there is no membrane to form a gradient across.

The inactivation parameter (ε), which occurs only on the $S_3 \rightarrow S_4$ transition, increases in discrete steps with plateaus in synchrony with the three phases of O_2 yield as the pool of available acceptors decrease. It is 5 times larger with FeCN alone than when PPBQ is added. We note that addition of more acceptor fully restores the O_2 yield- so this inactivation is non-destructive—unlike photoinactivation attributed to protein damage mainly to PSII D1. It does not parallel the semiquinone population of either the Q_B or Q_C sites, but instead parallels the population of the reduced pool of terminal electron acceptors. This is the expected behavior for inactivation caused by auto-reduction of the WOC or Y_z^+ by diffusion of semiquinone/quinol ($PPBQ^-$ or $PPBQH_2$) as these accumulate under illumination (Yanykin et al. 2010, 2017) (Oja and Laisk 2020) or by blocking of charge separation by stable reduction of Q_A. The former auto-reduction mechanism is seen in photoassembly experiments and as expected depends on the choice of the quinone electron acceptor (Gates et al. 2022).

This short-circuiting caused by diffusion of quinols from acceptor to donor side implies that longer range diffusion of PPBQ and FeCN molecules from outside to inside the microcrystals (~ 10–12 µm diameter) should also limit the yield of O_2. This phenomenon appears to be responsible for the large increase of O_2 yield with increasing dark time between flashes (Fig. 3). Faster flash rates produce substantially less O_2. The peak position (period) and the halfwidth of the "period-4" feature are seen to be essentially independent of the flash frequency, even though the yield of O_2 increases by a factor of almost 4 for a fourfold decrease in flash frequency. This outcome is consistent with rate-limiting diffusion of the terminal acceptor inside the microcrystals to capture more electrons. This phenomenon cannot be explained by eitherα, δ, or ε type processes (Mani et al. 2022; Kato et al. 2018; Pham and Messinger 2016).

By contrast, the period-2 amplitude decreases and the halfwidth increases at slower flash frequencies relative to the period-4 amplitude. This indicates that passage of electrons through the Q_B site into the terminal pool changes probability and shifts to a broader range of flash frequencies on the time scale of the measurement (1 to 4 s). The physical origin of this is unknown, but we postulate it may be caused by the uptake of a proton in anticipation of forming the hydrosemiquinone form, or the relaxation of the coordination environment around the charge on Q_B^-. Both mechanisms could produce a change in the probability of electron capture on the next flash. Such a mechanism might explain the presence of the satellite peak in the Fourier transform at period 4.0/4.7 (Fig. 2). This would correspond to preferred populations of Q_B^- with 0/1 or 1/2 H^+ loaded in the proton transfer site that functions in formation of the product $(QH_2)_B$. The protonation hypothesis is included in our proposed mechanism for PSII-CEF (Scheme 2) as it fits with the evidence for the switch between LEF and CEF.

Finally, we offer an explanation for the systematic change in resting populations of S-states measured at the end of each flash train and the intervening dark period (Fig. 6). The initial distribution S0:S1:S2 = 0.2:0.6:0.2 remains constant in phase 1 then changes to 0:0.95:0 at the end of phase 2, and finally in phase 3 small changes in both the S1 population decreases while S2 recovers. These changes are not attributable to the known decay lifetimes of these S-states in PSIX crystals in the absence of added quinone acceptors where the upper S states have very long lifetimes (Ananyev et al. 2019; Gates et al. 2022). Rather, these changes reflect shifts in the resting populations from longer-term pre-dark-adapted samples at time zero to shorter-term dark-adapted samples between trains. The shift to predominantly S1 as the major resting population reflects the effect of illumination and the shorter dark adaptation time between trains. Flashing will populate more of the higher S states, but the more reactive ones will disappear from the resting populations once the flashing stops. As a result, the shifted populations should not be the same as the steady-state dark populations. In the absence of external acceptors, the S2 state in PSIIX has a 10X longer decay time than does S3 (Ananyev et al. 2019; Gates et al. 2022). Nevertheless, it is highly oxidizing. Neither S2 nor S3 should be present between trains as these will react more rapidly with the native acceptors or with the added electron acceptors (more slowly by diffusion). This model predicts that S2 and S3 should disappear from the resting populations in favor of S1 and S2, respectively, since these will undergo auto-reduction if there is a semiquinone in the Q_B site but not in the Q_C site since this binds a proton to form the stable hydrosemiquinone $Q_C^-H^+$. This is precisely what the model in Scheme 2 predicts during phase 2. There is no resting S3 in the long-term dark-adapted sample, hence S2 can only disappear during phase 2. The model in Scheme 2 predicts that at the end of phase 2/start of phase 3 all S2 should be gone and S1 should reach its maximum population, as observed. As phase 3 continues there is only one microstate that can form once all terminal electron acceptor molecules are used up and only QH_2 remains in the pool. This state has an empty B site since QH_2 has low affinity, and a protonated semiquinone $Q_C^-H^+$. As this population replaces the previous one and Q_B^- disappears, the auto-reduction of

S2 disappears and the model predicts that the resting S2 population should recover at the expense of loss of S1. These predictions match the experimentally observed behavior in all three temporal phases of Fig. 6.

Conclusion

We provide new evidence for a molecular mechanism for PSII-cyclic electron flow that can account for the switch from LEF to CEF within PSII as the downstream pool of electron/proton carriers—the PQ/PQH_2 pool—responds to metabolic needs and environmental input. The model addresses both parameterized and model-independent observations of oxygen evolution in PSIIX. This model relies on a regulatory Q_C site which can exist in two redox states, $(Q^-/Q)_C$*nH^+, which are in equilibrium with the Q_B site $(Q/Q^-/Q^{2-})_B$*mH^+. This Q_C site responds to both the proton gradient across the thylakoid membrane and the redox poise of the downstream PQ pool via its equilibrium with the more redox-active and more easily protonated Q_B site. Upon forming the CEF microstate S_2(or S_3)$(Q^-)_C$*H^+, photochemical primary charge separation($P^+Q_A^-$) no longer forms $(QH_2)_B$ but instead undergoes a two-electron backward transition in which the two protons from the Q_C site are pumped into the lumen while the electrons return to the WOC forming S_1 (or S_2). The net outcome of this process is: 1) the conversion of redox energy accumulated in the PQH_2 pool into a *pmf* across the thylakoid membrane and ultimately into ATP, 2) restoring photochemical quenching by opening closed PSII centers that have over reduced PQH_2 pools, and 3) protecting against oxidative damage caused by the two most reactive S states (S3 and S4). Lastly, there is another functional role which PSII-CEF plays that allows operation of the Q-cycle which powers conventional PSI-dependent CEF. By oxidizing PQH_2 when the pool is over reduced, PSII-CEF regenerates PQ that is indispensable to operate the Q-cycle at the Q_i site of cytochrome b_6f. Without Q_i-PQ there is no PSI-CEF; only LEF through cytochrome b_6f can then occur. PSII-CEF is therefore needed to enable PSI-CEF whenever respiratory oxidation of PQH_2 is insufficient, e.g., under hypoxic conditions.

Supplementary Information The online version contains supplementary material available at https://doi.org/10.1007/s11120-022-00985-w.

Acknowledgements This work was funded by the Department of Energy, Basic Energy Sciences, Grant DE-FG02-10ER16195 (to G.C.D. and G.A.) and the NSF Science and Technology BioXFEL center award 1231306 (to P.F.).

Funding Basic Energy Sciences, DE-FG02-10ER16195,G. Charles Dismukes,BioXFEL Science and Technology Center, 1231306, Petra Fromme

Data availability All supporting data is available from C.G. or G.C.D. on request.

References

Amesz J (1964) Spectrophotometric evidence for the participation of a quinone in photosynthesis of intact blue-green algae. Biochim et Biophys Acta (BBA) Spec Sec Biophys Subj 79(2):257–265

Ananyev G, Dismukes GC (2005) How fast can Photosystem II split water? kinetic performance at high and low frequencies. Photosynth Res 84(1–3):355–365. https://doi.org/10.1007/s11120-004-7081-1

Ananyev G, Carrieri D, Dismukes GC (2008) Optimizing metabolic capacity and flux through environmental cues to maximize hydrogen production by cyanobacterium arthrospira maxima. Appl Environ Microbiol 74(19):6102–6113

Ananyev G, Gates C, Dismukes GC (2017a) The multiplicity of roles for (Bi)carbonate in photosystem II operation in the hypercarbonate-requiring cyanobacterium arthrospira maxima. Photosynthetica 56:217–228

Ananyev G, Gates C, Kaplan A (1858b) Dismukes GC (2017b) Photosystem II-cyclic electron flow powers exceptional photoprotection and record growth in the microalga Chlorella ohadii. Biochim et Biophys Acta (BBA)-Bioenerg 11:873–883. https://doi.org/10.1016/j.bbabio.2017b.07.001

Ananyev G, Gates C, Dismukes GC (2016) The oxygen quantum yield in diverse algae and cyanobacteria is controlled by partitioning of flux between linear and cyclic electron flow within photosystem II. Biochem Biophys Acta 1857:1380–1391

Ananyev G, Roy-Chowdhury S, Gates C, Fromme P, Dismukes GC (2019) The catalytic cycle of water oxidation in crystallized photosystem II complexes: performance and requirements for formation of intermediates. ACS Catal 9(2):1396–1407. https://doi.org/10.1021/acscatal.8b04513

Belyaeva NE, Schmitt F-J, Steffen R, Paschenko VZ, Riznichenko GY, Chemeris YK, Renger G, Rubin AB (2008) PS II model-based simulations of single turnover flash-induced transients of fluorescence yield monitored within the time domain of 100 ns–10 s on dark-adapted Chlorella pyrenoidosa cells. Photosynth Res 98(1):105–119. https://doi.org/10.1007/s11120-008-9374-2

Belyaeva NE, Bulychev AA, Riznichenko GY, Rubin AB (2019) Analyzing both the fast and the slow phases of chlorophyll a fluorescence and P700 absorbance changes in dark-adapted and preilluminated pea leaves using a Thylakoid Membrane model. Photosynth Res 140(1):1–19. https://doi.org/10.1007/s11120-019-00627-8

Bouges-Bocquet B (1980) Kinetic models for the electron donors of photosystem II of photosynthesis. Biochim Biophys Acta 594(2–3):85–103

Causmaecker SD, Douglass JS, Fantuzzi A, Nitschke W, Rutherford AW (2019) Energetics of the exchangeable quinone, Q_B, in Photosystem II. Proc Natl Acad Sci 116(39):19458–19463. https://doi.org/10.1073/pnas.1910675116

Coe J, Kupitz C, Basu S, Conrad CE, Roy-Chowdhury S, Fromme R, Fromme P (2015) Chapter twenty-two-crystallization of photosystem II for time-resolved structural studies using an X-ray free electron laser. Methods Enzymol 557:459–482

Crane F, Ehrlich B, Kegel L (1960) Plastoquinone reduction in illuminated chloroplasts. Biochem Biophys Res Commun 3(1):37–40

Dau H (1994) Molecular mechanisms and quantitative models of variable photosystem II fluorescence. Photochem Photobiol 60:1–23

Dau H, Haumann M (2007) Time-resolved X-ray spectroscopy leads to an extension of the classical S-state cycle model of photosynthetic oxygen evolution. Photosynth Res 92(3):327–343. https://doi.org/10.1007/s11120-007-9141-9

Dismukes GC, Siderer Y (1981) Intermediates of a polynuclear manganese center involved in photosynthetic oxidation of water. Proc Natl Acad Sci 78(1):274–278. https://doi.org/10.1073/pnas.78.1.274

Falkowski P, Fujita Y, Ley A, Mauzerall D (1986) Evidence for cyclic electron flow around photosystem II in Chlorella pyrenoidosa. Plant Physiol 81(1):310

Feikema WO, Marosvolgyi MA, Lavaud J, van Gorkom HJ (2006) Cyclic electron transfer in photosystem II in the marine diatom Phaeodactylum tricornutum. BBA-Bioenergetics 1757(7):829–834. https://doi.org/10.1016/j.bbabio.2006.06.003

Gates C, Ananyev G, Dismukes GC (2016) The strontium inorganic mutant of the water oxidizing center (CaMn4O5) of PSII improves WOC efficiency but slows electron flux through the terminal acceptors. Biochim et Biophys Acta (BBA)-Bioenerg 1857(9):1550–1560. https://doi.org/10.1016/j.bbabio.2016.06.004

Gates C, Ananyev G, Roy-Chowdhury S, Cullinane B, Miller M, Fromme P, Dismukes GC (2022) Why did nature choose manganese over cobalt to make oxygen photosynthetically on the earth? J Phys Chem B 126(17):3257–3268

Guskov A, Kern J, Gabdulkhakov A, Broser M, Zouni A, Saenger W (2009) Cyanobacterial Photosystem II at 29-angstrom resolution and the role of quinones, lipids, channels and chloride. Nat Struct Mol Biol 16(3):334–342. https://doi.org/10.1038/nsmb.1559

Hasegawa K, Noguchi T (2014) Molecular interactions of the quinone electron acceptors QA, QB, and QC in photosystem II as studied by the fragment molecular orbital method. Photosynth Res 120(1):113–123

Huang J-Y, Chiu Y-F, Ortega JM, Wang H-T, Tseng T-S, Ke S-C, Roncel M, Chu H-A (2016) Mutations of cytochrome b 559 and PsbJ on and near the QC site in Photosystem II influence the regulation of short-term light response and photosynthetic growth of the cyanobacterium Synechocystis sp. PCC 6803. Biochemistry 55(15):2214–2226

Jenson DL, Barry BA (2009) Proton-coupled electron transfer in photosystem II: proton inventory of a redox active tyrosine. J Am Chem Soc 131(30):10567–10573. https://doi.org/10.1021/ja902896e

Joliot P, Joliot A (1968) A polarographic method for detection of oxygen production and reduction of Hill reagent by isolated chloroplasts. Biochim et Biophys Acta (BBA)-Bioenerg 153(3):625–634

Joliot P, Barbieri G, Chabaud R (1969) A new model of photochemical centers in system-2. Photochem Photobiol 10(5):309–329

Kato Y, Akita F, Nakajima Y, Suga M, Umena Y, Shen J-R, Noguchi T (2018) Fourier transform infrared analysis of the S-state cycle of water oxidation in the microcrystals of photosystem II. J Phys Chem Lett 9(9):2121–2126

Kedem I, Milrad Y, Kaplan A, Yacoby I (2021) Juggling lightning: how Chlorella ohadii handles extreme energy inputs without damage. Photosynth Res 147(3):329–344

Kok B, Forbush B, McGloin M (1970) Cooperation of charges in photosynthetic oxygen evolution part 1: a linear 4 step mechanism. Photochem Photobiol 11(6):457–475. https://doi.org/10.1111/j.1751-1097.1970.tb06017.x

Krivanek R, Kern J, Zouni A, Dau H, Haumann M (2007) Spare quinones in the QB cavity of crystallized photosystem II from Thermosynechococcus elongatus. Biochim et Biophys Acta (BBA)-Bioenerg 1767(6):520–527

Kupitz C, Basu S, Grotjohann I, Fromme R, Zatsepin NA, Rendek KN, Hunter MS, Shoeman RL, White TA, Wang D (2014a) Serial time-resolved crystallography of photosystem II using a femtosecond X-ray laser. Nature 513(7517):261–265

Kupitz C, Grotjohann I, Conrad CE, Roy-Chowdhury S, Fromme R, Fromme P (2014b) Microcrystallization techniques for serial femtosecond crystallography using photosystem II from Thermosynechococcus elongatus as a model system. Phil Trans R Soc B 369(1647):20130316

Laisk A, Oja V (2018) Kinetics of photosystem II electron transport: a mathematical analysis based on chlorophyll fluorescence induction. Photosynth Res 136(1):63–82. https://doi.org/10.1007/s11120-017-0439-y

Lambreva MD, Russo D, Polticelli F, Scognamiglio V, Antonacci A, Zobnina V, Campi G, Rea G (2014) Structure/function/dynamics of photosystem II plastoquinone binding sites. Curr Protein Pept Sci 15(4):285–295

Lavergne J, Junge W (1993) Proton release during the redox cycle of the water oxidase. Photosynth Res 38(3):279–296. https://doi.org/10.1007/bf00046752

Lazár D, Jablonský J (2009) On the approaches applied in formulation of a kinetic model of photosystem II: different approaches lead to different simulations of the chlorophyll a fluorescence transients. J Theor Biol 257(2):260–269

Mani K, Zournas A, Dismukes GC (2022) Bridging the gap between Kok-type and kinetic models of photosynthetic electron transport within Photosystem II. Photosynth Res 151(1):83–102. https://doi.org/10.1007/s11120-021-00868-6

Manoj KM, Gideon DA, Parashar A, Nirusimhan V, Annadurai P, Jacob VD, Manekkathodi A (2021) Validating the predictions of murburn model for oxygenic photosynthesis: Analyses of ligand-binding to protein complexes and cross-system comparisons. J Biomol Struct Dyn. https://doi.org/10.1080/07391102.2021.1953607

Meunier PC (1993) Oxygen evolution by photosystem II: the contribution of backward transitions to the anomalous behaviour of double-hits revealed by a new analysis method. Photosynth Res 36(2):111–118

Meunier P, Burnap R (1996) Improved 5-step modeling of the Photosystem II S-state mechanism in cyanobacteria. Photosynth Res 47(1):61–76

Oja V, Laisk A (2020) Time-and reduction-dependent rise of photosystem II fluorescence during microseconds-long inductions in leaves. Photosynth Res 145(3):209–225

Pham LV, Messinger J (2014) Electrochemically produced hydrogen peroxide affects Joliot-type oxygen-evolution measurements of photosystem II. Biochim et Biophys Acta (BBA)-Bioenerg 1837(9):1411–1416. https://doi.org/10.1016/j.bbabio.2014.01.013

Pham LV, Messinger J (2016) Probing S-state advancements and recombination pathways in photosystem II with a global fit program for flash-induced oxygen evolution pattern. Biochim et Biophys Acta (BBA)-Bioenerg 1857(6):848–859. https://doi.org/10.1016/j.bbabio.2016.03.013

Pham LV, Janna Olmos JD, Chernev P, Kargul J, Messinger J (2019) Unequal misses during the flash-induced advancement of photosystem II: effects of the S state and acceptor side cycles. Photosynth Res 139(1):93–106

Prasil O, Kolber Z, Berry J, Falkowski P (1996) Cyclic electron flow around photosystem II in vivo. Photosynth Res 48(3):395–410

Rappaport F, Guergova-Kuras M, Nixon PJ, Diner BA, Lavergne J (2002) Kinetics and pathways of charge recombination in photosystem II. Biochemistry 41(26):8518–8527

Robinson HH, Crofts AR (1983) Kinetics of the oxidation—reduction reactions of the photosystem II quinone acceptor complex, and the pathway for deactivation. FEBS Lett 153(1):221–226

Satoh K, Koike H, Ichimura T, Katoh S (1992) Binding affinities of benzoquinones to the QB site of Photosystem II in Synechococcus oxygen-evolving preparation. Biochim et Biophys Acta

(BBA)-Bioenerg 1102(1):45–52. https://doi.org/10.1016/0005-2728(92)90063-8
Schatz GH, Brock H, Holzwarth AR (1988) Kinetic and energetic model for the primary processes in photosystem II. Biophys J 54(3):397–405. https://doi.org/10.1016/S0006-3495(88)82973-4
Shinkarev V (1996) Binary oscillations in the Kok model of oxygen evolution in oxygenic photosynthesis. Photosynth Res 48(3):411–417. https://doi.org/10.1007/BF00029473
Shinkarev VP (2003) Oxygen evolution in photosynthesis: simple analytical solution for the Kok model. Biophys J 85(1):435–441
Shinkarev V (2005a) Flash-induced oxygen evolution in photosynthesis: simple solution for the extended s-state model that includes misses, double hits, inactivation, and backwards transitions. Biophys J 88:412–421
Shinkarev VP (2005b) Flash-induced oxygen evolution and other oscillation processes in Photosystem II. In: Wydrzynski T, Satoh K (eds) Photosystem II: The Water/Plastoquinone Oxido-Reductase In Photosynthesis. Klewer Academic Publishers, The Netherlands
Shinkarev VP, Wraight CA (1993a) Kinetic factors in the bicycle model of oxygen evolution by Photosystem II. Photosynth Res 38(3):315–321. https://doi.org/10.1007/BF00046756
Shinkarev VP, Wraight CA (1993b) Oxygen evolution in photosynthesis: from unicycle to bicycle. Proc Natl Acad Sci USA 90(5):1834–1838
Shinopoulos KE, Brudvig GW (2012) Cytochrome b 559 and cyclic electron transfer within photosystem II. Biochim et Biophys Acta (BBA)-Bioenerg 1817(1):66–75
Steffen M (1990) A simple method for monotonic interpolation in one dimension. Astron Astrophys 239:443
Swarztrauber PN (1982) Vectorizing the FFTs. In: Rodrigue G (ed) Parallel Computations". Academic Press, Cambridge
Takagi D, Ifuku K, Nishimura T, Miyake C (2019) Antimycin A inhibits cytochrome b559-mediated cyclic electron flow within photosystem II. Photosynth Res 139(1):487–498
Vass I (2012) Molecular mechanisms of photodamage in the Photosystem II complex. Biochim et Biophys Acta (BBA)-Bioenerg 1817(1):209–217
Vass I, Cser K (2009) Janus-faced charge recombinations in photosystem II photoinhibition. Trends Plant Sci 14(4):200–205
Vinyard DJ, Zachary CE, Ananyev G (1827) Dismukes GC (2013) Thermodynamically accurate modeling of the catalytic cycle of photosynthetic oxygen evolution: a mathematical solution to asymmetric Markov chains. Biochim Biophys Acta 7:861–868. https://doi.org/10.1016/j.bbabio.2013.04.008
Wraight C (1979) Electron acceptors of bacterial photosynthetic reaction centers II. H+ binding coupled to secondary electron transfer in the quinone acceptor complex. Biochim et Biophys Acta (BBA)-Bioenerg 548(2):309–327
Yadav DK, Prasad A, Kruk J, Pospíšil P (2014) Evidence for the involvement of loosely bound plastosemiquinones in superoxide anion radical production in photosystem II. PLoS ONE 9(12):e115466. https://doi.org/10.1371/journal.pone.0115466
Yanykin DV, Khorobrykh AA, Khorobrykh SA, Klimov VV (2010) Photoconsumption of molecular oxygen on both donor and acceptor sides of photosystem II in Mn-depleted subchloroplast membrane fragments. Biochim et Biophys Acta (BBA)-Bioenerg 1797(4):516–523
Yanykin D, Khorobrykh A, Terentyev V, Klimov V (2017) Two pathways of photoproduction of organic hydroperoxides on the donor side of photosystem 2 in subchloroplast membrane fragments. Photosynth Res 133(1):129–138
Yao M, Liu Y, Fei L, Zhou Y, Wang F, Chen J (2018) Self-adaptable quinone–quinol exchange mechanism of photosystem II. J Phys Chem B 122(46):10478–10489
Zhu X-G, Baker NR, Ort DR, Long SP (2005) Chlorophyll a fluorescence induction kinetics in leaves predicted from a model describing each discrete step of excitation energy and electron transfer associated with photosystem II. Planta 223(1):114–133

Authors and Affiliations

Colin Gates[1,2,3,4] · Gennady Ananyev[1,2] · Shatabdi Roy-Chowdhury[5] · Petra Fromme[5] · G. Charles Dismukes[1,2]

[1] Dept of Chemistry & Chemical Biology, Rutgers University, Piscataway, USA

[2] Waksman Institute of Microbiology, Rutgers University, Piscataway, USA

[3] Dept of Computational Biology & Molecular Biophysics, Rutgers University, Piscataway, NJ, USA

[4] Dept of Chemistry and Biochemistry, Loyola University Chicago, Chicago, IL, USA

[5] Center for Applied Structural Discovery, Biodesign Institute, Arizona State University, Tempe, AZ, USA